IVYSPRING INTERNATIONAL PUBLISHER

Theranostics

2018; 8(4): 955-971. doi: 10.7150/thno.22325

Research Paper

All-in-One Theranostic Nanoplatform Based on Hollow MoS_x for Photothermally-maneuvered Oxygen Self-enriched Photodynamic Therapy

Jinping Wang, Li Liu, Qing You, Yilin Song, Qi Sun, Yidan Wang, Yu Cheng, Fengping Tan, Nan Li✉

Tianjin Key Laboratory of Drug Delivery & High-Efficiency, School of Pharmaceutical Science and Technology, Tianjin University, 300072, Tianjin, PR China.

✉ Corresponding author: School of Pharmaceutical Science and Technology, Tianjin University, 300072, Tianjin, PR China. Tel.:+86-022-27404986 E-mail address: linan19850115@163.com

Received: 2017.08.11; Accepted: 2017.10.15; Published: 2018.01.01

Abstract

Photodynamic therapy (PDT) kills cancer cells by converting tumor-dissolved oxygen into reactive singlet oxygen ($^1O_2$) using a photosensitizer under laser irradiation. However, pre-existing hypoxia in tumors and oxygen consumption during PDT can result in an inadequate oxygen supply, which in turn hampers PDT efficacy. Herein, an O_2 self-sufficient nanotheranostic platform based on hollow MoS_x nanoparticles ($HMoS_x$) with oxygen-saturated perfluorohexane (O_2@PFH) and surface-modified human serum albumin (HSA)/chloride aluminium phthalocyanine (AlPc) (O_2@PFH@$HMoS_x$-HSA/AlPc), has been designed for the imaging and oxygen self-enriched photodynamic therapy (Oxy-PDT) of cancer.

Methods: The *in vitro* anti-cancer activity and intracellular $^1O_2$ generation performance of the nanoparticles were examined using 4T1 cells. We also evaluated the multimodal imaging capabilities and anti-tumor efficiency of the prepared nanoparticles in vivo using a 4T1 tumor-bearing nude mouse model.

Results: This nanoplatform could achieve the distinct *in vivo* fluorescence (FL)/photoacoustic (PA)/X-ray computed tomography (CT) triple-model imaging-guided photothermally-maneuvered Oxy-PDT. Interestingly, the fluorescence and Oxy-PDT properties of O_2@PFH@$HMoS_x$-HSA/AlPc were considerably quenched; however, photothermal activation by 670 nm laser irradiation induced a significant increase in temperature, which empowered the Oxy-PDT effect of the nanoparticles. In this study, O_2@PFH@$HMoS_x$-HSA/AlPc demonstrated a great potential to image and treat tumors both *in vitro* and *in vivo*, showing complete tumor-inhibition over 16 days after treatment in the 4T1 tumor model.

Conclusion: O_2@PFH@$HMoS_x$-HSA/AlPc is promising to be used as novel multifunctional theranostic nanoagent for triple-modal imaging as well as single wavelength NIR laser triggered PTT/Oxy-PDT synergistic therapy.

Key words: Hollow structure, Theranostic nanoagent, Triple-modal imaging, Photothermally maneuvered, Oxygen self-enriched photodynamic therapy.

Introduction

Photodynamic therapy (PDT), which utilizes singlet oxygen ($^1O_2$) generated from photosensitizers (PS) and tumor-dissolved oxygen (O_2) under laser irradiation to kill cells, has attracted tremendous attention for cancer treatment [1, 2]. However, the effectiveness of PDT is severely impaired by the intrinsic hypoxic tumor microenvironment ($pO_2 \leq 2.5$ mmHg) [3, 4]. What's more, the constant O_2 consumption mediated by PS during the PDT process further worsens tumor hypoxia and greatly limits PDT efficiency [5]. To address this challenge, different strategies have been proposed to modify the hypoxic tumor microenvironment by promoting the oxygenation of tumors to achieve better PDT therapeutic outcomes [6-8]. Several studies have reported that the tumor hypoxia could be relieved by the ability of catalase or manganese dioxide (MnO_2) nanoparticles to trigger the decomposition of

endogenous hydrogen peroxide (H_2O_2) existing inside the tumor to produce O_2 in situ, realizing significantly promoted treatment outcomes of PDT [9, 10]. In our recent work, it was found that the mild photothermal effect induced by near-infrared (NIR)-light-absorbing nanoparticles could be utilized to increase intratumoral blood flow and subsequently improve the oxygenation status of the tumor microenvironment [11]. However, the tumor reoxygenation levels were still limited by either the amount of available H_2O_2 existing in the tumor microenvironment or the oxygen delivery capability of red blood cells reaching the tumor blood vessels. Thus, there is an urgent need to develop a smart delivery system with sufficient O_2 supply to realize a highly effective oxygen self-enriched photodynamic therapy (Oxy-PDT) under the native tumor hypoxic microenvironment.

Perfluorohexane (PFH), which is a kind of liquid perfuorocarbon, can dissolve a large amount of oxygen and serve as an oxygen carrier, enabling it to be used as a blood substitute [12, 13]. To date, many formulations of liquid perfuorocarbon have been extensively used in the clinic as artificial blood substitutes due to their great biocompatibility and high oxygen-affinity [12-14]. For instance, Oxypherol (Fluosol-43) has obtained FDA approval in improving myocardial oxygenation and preventing abnormalities in ventricular function [15]. In a recent work, it was proposed that photosensitizer-coupled PFH nanoparticles could be used as an adjuvant treatment to increase the therapeutic outcome of PDT via dragging oxygen molecules close to photosensitizers [16]. Moreover, it has been reported that the $^1O_2$ lifetime in PFH is much longer than in the cellular environment or in water [17], which results in long-lasting PDT effects. Although PFH possesses high oxygen solubility, it releases oxygen simply by diffusion through the oxygen concentration gradient, thus leading to leaking of oxygen in the blood circulation [18, 19]. Liu's group recently found that NIR laser mediated photothermal effect could be utilized to trigger the timely release of oxygen from PFH loaded nanostructures, subsequently contributing to remarkably enhanced radiotherapeutic efficacy [20]. Thus, a well-designed NIR laser-absorbing theranostic nanocarrier is needed to simultaneously carry oxygen saturated PFH and photosensitizer for accurate and optimized Oxy-PDT treatment of tumor.

In our previous work, MoS_2 nanodot@ polyaniline nanohybrids, which were able to absorb NIR light and X-ray irradiation, were used for combined photothermal therapy and radiotherapy of tumors [21]. Based on this previous study, we optimized the MoS_2 nanodots into hollow MoS_x nanoparticles ($HMoS_x$) by a facile strategy using NH_3 bubble as a soft template. The hollow structure could be effectively filled with PFH, which is then able to act as an oxygen reservoir. Additionally, the large surface areas of both the exterior and interior of the hollow nanostructure could increase the amount of light absorbed, thus improving the photothermal effect [22, 23]. As a typical nonstoichiometric metal chalcogenide, $HMoS_x$ nanoparticle was first proposed for use in cancer photothermal therapy (PTT) and photoacoustic (PA) imaging owing to its strong absorbance in the NIR region. In addition, MoS_x is also promising for biomedical applications as an X-ray computed tomography (CT) imaging contrast agent given the high X-ray attenuation coefficient of Mo [21]. HSA, as an endogenous protein approved by FDA for intravenous administration [24], was used to modify the $HMoS_x$ nanoparticles ($HMoS_x$-HSA). What's more, HSA coated nanoparticles have been shown to possess both passive and active tumor-targeting abilities via enhanced permeability and retention (EPR) effect as well as gp60/SPARC receptor-mediated transcytosis, respectively [25]. Next, chloride aluminium phthalocyanine (AlPc) PSs were modified to endow $HMoS_x$-HSA ($HMoS_x$-HSA/AlPc) with the ability to produce reactive oxygen species (ROS) when excited by NIR laser irradiation.

Herein, we demonstrated the potential of O_2@PFH@$HMoS_x$-HSA/AlPc as a theranostic nanoplatform for fluorescence (FL)/PA/CT multi-modal imaging and NIR laser triggered PTT/Oxy-PDT synergistic therapy (Scheme 1). Under the single wavelength NIR laser irradiation (670 nm), photothermal effect induced by $HMoS_x$ could produce significant increases in local temperature. Then, the soaring heat, which could reach the boiling point of PFH, markedly accelerated AlPc and O_2 release from O_2@PFH@$HMoS_x$-HSA/AlPc and thus promptly activated the Oxy-PDT effect (Figure 2A). The smart O_2@PFH@$HMoS_x$-HSA/AlPc nanoparticles possess multiple unique advantages. (1) Oxygen self-enriched property: O_2@PFH@$HMoS_x$-HSA/AlPc could carry oxygen into the tumor site, allowing activatable oxygen release in the hypoxic tumor environment to enhance the PDT effect. (2) Stimuli response: AlPc/O_2 release and the subsequent Oxy-PDT could be photothermally maneuvered under single wavelength NIR laser irradiation. (3) Multifunction: O_2@PFH@$HMoS_x$-HSA/AlPc could serve as a multifunctional platform to integrate complementary imaging modalities and synergistic PTT/Oxy-PDT therapeutic strategies together. Thus, our O_2@PFH@$HMoS_x$-HSA/AlPc would be a promising

agent for tumor hypoxia modulation and triple-modality imaging-guided PTT/Oxy-PDT synergistic cancer treatment with enhanced tumor inhibition efficacy.

Materials and Methods

Materials

Ammonium tetrathiomolybdate ($(NH_4)_2MoS_4$) and 1,3-Diphenylisobenzofuran (DPBF) were purchased from Heowns Biochem Technologies LLC (Tianjin, China). Hydrazine hydrate ($N_2H_4.H_2O$) was obtained from Adamas Reagent Co., Ltd. (Shanghai, China). Perfuorohexane was purchased from Xianding Biological Technology co., Ltd. (Shanghai, China). Human serum albumin (HSA) and calcein-AM/PI double stain kit were received from Sigma-Aldrich (USA). Lipoic acid (LA) and 1-ethyl-3(3-(dimethylamino)-propyl) carbodiimide·hydrochloride (EDC·HCl) were purchased from Shanghai Macklin Biochemical Co., Ltd. Chloride aluminium phthalocyanine (AlPc) was obtained from Shanghai Meryer Co., Ltd. All other chemicals were analytical grade and used as received.

Synthesis of $HMoS_x$-HSA/AlPc

Firstly, $HMoS_x$ nanoparticles were prepared by the hydrothermal process, as previously reported [26]. In a typical procedure, 0.5 mmol of $(NH_4)_2MoS_4$ was added to a 200 mL beaker with 80 mL of NMP. After sonicating for 3 h, the obtained clear solution was poured into a 250 mL three-necked flask. Then, 5.0 mL of $N_2H_4·H_2O$ was added to the flask dropwise under magnetic stirring. Afterwards, the reaction mixture was heated to 80 °C in an oil bath and constantly stirred for 12 h under gentle reflux. After being naturally cooled, the black-brown precipitates were collected by centrifugation at 7200 × g, washed sequentially with ethanol and deionized water 3 times. Then, the obtained precipitates were dried in a vacuum chamber overnight. Finally, the as-prepared hollow MoS_x nanosphere ($HMoS_x$) powder was collected for further use.

Secondly, to enhance the water-soluble property of the synthesized $HMoS_x$, the HSA protein was coated on the surface of $HMoS_x$. In a typical synthesis, $HMoS_x$ sample was firstly coated with lipoic acid (LA) according to the following process: 80 mg of LA was added into 4 mL of $HMoS_x$ (2 mg/mL) by sonication for 5 h. Then, the obtained LA-coated $HMoS_x$ nanoparticles were collected by centrifuging at 7200 × g for 10 min. Next, to conjugate HSA to LA-coated $HMoS_x$, 80 mg HSA was mixed with 4 mL aqueous solution of LA-coated $HMoS_x$ (2 mg/mL) and then 4 mg of EDC was added. The solution was then stirred at room temperature for 2 h, added with another 4 mg of EDC, and then further stirred for 6 h. The obtained $HMoS_x$-HSA nanoparticles were collected by centrifuging at 7200 × g for 10 min. Then, the obtained precipitate was re-dispersed in deionized water and stored at 4 °C for further use.

Thirdly, for AlPc loading, a predetermined amount of AlPc in 1 mL of DMSO/distilled water (1:1, v/v) was slowly added to $HMoS_x$-HSA solution (10 mg in 10mL DMSO/distilled water). Afterward, the solution was sonicated for 5 min and stirred at room temperature for 24 h. After centrifuging (7200 × g, 10 min) and washing with water 3 times to remove unloaded AlPc, the product was lyophilized to obtain green powder ($HMoS_x$-HSA/AlPc).

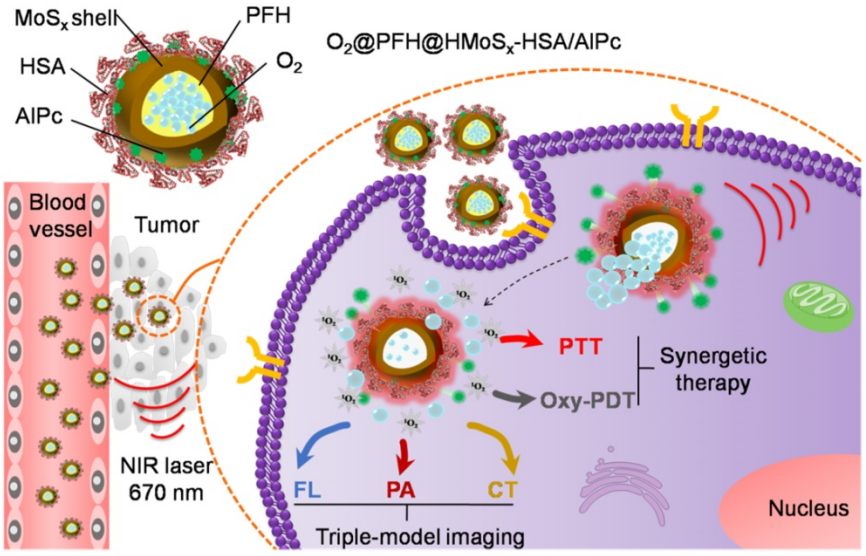

Scheme 1. Schematic illustration of O_2@PFH@$HMoS_x$-HSA/AlPc theranostic nanoagents for in vivo FL/PA/CT imaging and NIR laser triggered PTT/Oxy-PDT synergistic therapy of tumors.

PFH loading, oxygen saturation, and measurement of O_2 release

The PFH loading process was conducted according to a reported method [27]. After freeze-drying, the $HMoS_x$-HSA/AlPc sample (5 mg) was transferred into a 50 mL sealed bottle with rubber plug. After the air in the bottle was evacuated, 50 μL of PFH was injected. Then the bottle was sonicated in ice water for 5 min. 1 mL of PBS was injected into the bottle and further sonicated for 10 min. Next, 1 mL of PFH loaded $HMoS_x$-HSA/AlPc dispersed in PBS was placed in a 50 mL sample tube and stored in an aseptic oxygen chamber (O_2 flow rate = 5 L/min) for 15 min to achieve oxygen saturation. Finally, the oxygen-saturated, PFH-loaded $HMoS_x$-HSA/AlPc (O_2@PFH@$HMoS_x$-HSA/AlPc) was obtained.

The oxygen concentrations in aqueous solutions were measured using a portable dissolved oxygen meter (Rex, JPB-607A, China). For measurement of O_2 release, 15 mL of deoxygenated water placed in a 50 mL flask was filled with nitrogen. The oxygen electrode probe was inserted into the flask to measure the oxygen concentration of the solution in real time. Then, 5 mL of O_2@PFH@$HMoS_x$-HSA/AlPc or O_2@$HMoS_x$-HSA/AlPc solution (5 mg/mL) was injected into the flask. The oxygen concentration was recorded during all processes for 20 min (one measurement every 30 s). For the measurement of O_2 release triggered by NIR laser, the solution was irradiated by a 670 nm laser (1 W/cm²) for 10 min.

Material characterization

TEM images of the $HMoS_x$ were obtained by the JEM-100 CX (Jeol Ltd., Tokyo, Japan) instrument. Element mapping images and EDS line scanning results were obtained using a JEM-2100F (Jeol Ltd., Tokyo, Japan) transmission electron microscope. The XPS measurements were performed using a PHI-5000 CESCA system (PerkinElmer) with radiation from an Al Kα (1486.6 eV) X-ray source. The CD spectra of pure HSA and $HMoS_x$-HSA were collected using a spectropolarimeter system (BioLogic, MOS-450). The surface area and pore size of the nanoparticles were determined by Brunauer-Emmett-Teller (BET), nitrogen adsorption-desorption and Barrett-Joyner-Halenda (BJH) methods (Micromeritics, ASAP2020), respectively. UV-Vis spectra were measured by a Cary 60 UV-Vis spectrophotometer (Agilent, USA) using quartz cuvettes with an optical path of 1 cm. Fluorescence spectra of different samples were investigated by an LS-55 fluorescence spectrophotometer (Perkin-Elmer). Photothermal images were captured by a Ti32 infrared camera (Fluke TiR, USA) and analyzed by SmartView software. The excitation source was a 670 nm diode-pumped solid-state laser system (LASERGLOW Technologies, Shanghai, China). The *in vitro* CT images of various concentrations of $HMoS_x$-HSA/AlPc solution were acquired using a Gamma Medica-Ideas instrument. Meanwhile, different concentrations of $HMoS_x$-HSA/AlPc dissolved in purified water were used for in vitro PA signal detection.

To measure the photothermal conversion efficiency (η), the aqueous dispersion samples were exposed to 670 nm NIR laser (1.0 W/cm²) for 600 s, and then the laser was shut off. The photothermal conversion efficency was calculated according to the following equation:

$$\eta = [hS(T_{max} - T_{surr}) - Q_0] / [I(1 - 10^{-A670})] \quad (1)$$

Where h is the heat transfer coefficient, S is the sample container surface area, T_{max} is the steady state maximum temperature, T_{surr} is the ambient room temperature, Q_0 is the heat associated with the light absorbance of the solvent, which is measured using pure water, I is the laser power, and $A670$ is the absorbance of our nanoparticles at the wavelength of 670 nm.

In order to get the value of hS, θ herein is introduced, which is defined as the ratio of $(T - T_{surr})$ to $(T_{max} - T_{surr})$:

$$\theta = (T - T_{surr}) / (T_{max} - T_{surr}) \quad (2)$$

Thus, the value of hS is determined by Equation 3:

$$\tau_s = C_d m_d / hS \quad (3)$$

Where τ_s is the characteristic thermal time constant, the mass of the nanoparticle solution (m_d) is in g, and its heat capacity (C_d) is ~4.2 J g^{-1} k^{-1} (the heat capacity of pure water).

In vitro AlPc release test and singlet oxygen generation of O_2@PFH@$HMoS_x$-HSA/AlPc

The AlPc release behavior from $HMoS_x$-HSA/AlPc was investigated using a dialysis method. 1 mL of $HMoS_x$-HSA/AlPc was placed in a dialysis bag (MWCO = 14 kDa) and exposed with or without a 670 nm PTT laser at 0 and 0.5 h, respectively. At different time intervals, 2 mL of the receiving solution was collected and measured by the absorbance spectrometer to determine the concentrations of released drugs, and then poured back to ensure a constant volume. To quantitatively evaluate the generation of singlet oxygen, 1,3-diphenyl isobenzofuran (DPBF) was used in this study. A certain amount of O_2@PFH@$HMoS_x$-HSA/AlPc was mixed with DPBF (10 μM) in acetonitrile, followed by irradiaton with an NIR laser

(670 nm, 1 W/cm^2). The absorbance of the solution at 410 nm was monitored at different time points using a UV-vis spectrometer.

Cell culture in hypoxic and normoxic environments

4T1 cells were cultured in a DMEM medium in an atmosphere of 21% O_2 and 5% CO_2 at 37 °C to mimic the normoxic environment. For comparison, 1% O_2 and 5% CO_2 at 37 °C was used to mimic the hypoxic tumor microenvironment.

In vitro phototherapy

For cell cytotoxicity assay, 4T1 cells were seeded into 96-well plates (1 × 10^4 per well) until adherent and then incubated with different samples. After 6 h incubation, the cells were treated with or without 670 nm (1 W/cm^2, 3 min) irradiation. After another 18 h of incubation, the standard thiazolyl tetrazolium (MTT, Sigma-Aldrich) test was conducted to measure the cell viabilities relative to the untreated cells.

The synergistic PDT/PTT effects of O_2@PFH@HMoS$_x$-HSA/AlPc on 4T1 cells in the hypoxic tumor microenvironment were further verified using Calcein AM and propidium iodide (PI) co-staining. 4T1 cells (5 × 10^5 cells per well) were seeded in 6-well plates and incubated overnight at 37 °C in a humidified 1% O_2 and 5% CO_2 atmosphere. After being rinsed with PBS (pH 7.4), the cells were incubated with HMoS$_x$-HSA, HMoS$_x$-HSA/AlPc or O_2@PFH@HMoS$_x$-HSA/AlPc for 6 h under the same conditions, respectively. Afterward, the cells of the experimental group were rinsed again with PBS and immersed in 200 μL of fresh culture medium, and subsequently irradiated by a 670 nm laser (1 W/cm^2, 5 min). Then the cells were incubated for another 18 h. According to the manufacturer's suggested protocol, cells were digested and stained with calcein-AM and PI for visualization of live and dead/late apoptotic cells, respectively. Afterward, the cells of all groups were rinsed again with PBS and were observed by confocal fluorescence microscopy (Leica).

To determine the apoptotic and necrotic cell distributions, 4T1 cells were planted in 6-well plates at a concentration of 2 × 10^5 cells/well and incubated under the hypoxia conditions for 24 h. They were then incubated with 200 μg/mL HMoS$_x$-HSA, HMoS$_x$-HSA/AlPc and O_2@PFH@HMoS$_x$-HSA/AlPc for 24 h with or without 670 nm laser irradiation. After 24 h incubation, the cells were collected and stained with Annexin V/PI following the protocol of the kit, and then analyzed with flow cytometry.

ROS analysis

Intracellular ROS and hypoxia were explored using the ROS-ID Hypoxia/Oxidative stress detection kit (Enzo Life Sciences). 4T1 cells were cultured in a confocal dish (5 × 10^4 cells/dish) and grown in hypoxic or normoxic environment for 24 h. Then, cells were treated with HMoS$_x$-HSA/AlPc or O_2@PFH@HMoS$_x$-HSA/AlPc for 6 h and then administrated with the kit reagent mix according to the manufacturer's instructions. After 30 min, the cells were washed twice and exposed to 670 nm laser irradiation for 3 min. After that, cells were washed with PBS, stained by DAPI, and observed by confocal fluorescence microscopy (Leica).

Tumor animal model and in vivo infrared thermal imaging

All animals including female nude mice and Kunming mice were purchased from Huafukang Biological Technology Co. Ltd (Beijing, China). All animals were maintained in accordance with the guidelines of Tianjin University. Nude mice bearing 4T1 tumors were used for fluorescence imaging, infrared thermal imaging, and PA imaging. Kunming mice were used for histocompatibility investigation, biodistribution, and simultaneous PTT/PDT study. All animals in this work received humane care in compliance with the institution's guidelines for maintenance and use of laboratory animals in research. The 4T1 tumors were produced by subcutaneous injection of 4T1 cells (2 × 10^6) in about 50 μL PBS into the oxter of each mouse. Tumor size was measured periodically using a slide caliper. When tumor volumes approached ~100 mm^3, the mice were anaesthetized and then i.v. injected with PBS and HMoS$_x$-HSA/AlPc for infrared thermal imaging. Afterwards, the mice were imaged under NIR 670-nm laser irradiation for 5 min.

In vivo FL/PA/CT imaging

For *in vivo* fluorescence imaging, HMoS$_x$-HSA/AlPc (200 μL, 2 mg/mL) were i.v. injected into the tail vein of 4T1 tumor bearing Balb/c nude mice. The fluorescence images were acquired on an ex/in vivo imaging system (CRi, Woburn, MA). After the 24 h in vivo imaging, all mice were euthanized. Major organs including tumors were collected and subjected to ex vivo imaging.

For *in vivo* PA imaging, 4T1 tumor-bearing Balb/c nude mice were intravenously injected with 200 μL of HMoS$_x$-HSA/AlPc with a dose of 20 mg/kg. Next, the in vivo photoacoustic imaging was acquired on a Vevo LAZR PAI System.

For *in vivo* CT imaging, 4T1 tumor-bearing Balb/c nude mice were intratumorally injected with 50 μL of HMoS$_x$-HSA/AlPc (10 mg/mL). Before and after the injection, the mice were set on a small X-ray CT (Gamma Medica-Ideas) for imaging. The images

were scanned in the accurate mode using full angle, 3 frame averaging, 270 μA tube current, and 80 kV tube voltage. To measure the biodistribution of nanoparticles, tumors and major organs including heart, liver, spleen, lung and kidney from $HMoS_x$-HSA/AlPc solution treated mice were solubilized for ICP-MS measurement to determine tungsten levels after 4, 8, 12 and 24 h.

In vivo therapeutic efficacy

To evaluate the phototherapy effects of O_2@PFH@$HMoS_x$-HSA/AlPc, 4T1 tumor-bearing mice were randomly divided into six groups: (1) PBS, (2) O_2@PFH@$HMoS_x$-HSA/AlPc, (3) $HMoS_x$-HSA with 670 nm laser, (4) $HMoS_x$-HSA/AlPc with 670 nm laser, (5) O_2 @$HMoS_x$-HSA/AlPc with 670 nm laser, and (6) O_2@PFH@$HMoS_x$-HSA/AlPc with 670 nm laser. Each treatment was conducted at day 0 via tail-vein injection. Subsequently, phototherapy treatment (5 min, 670 nm, 1 W/cm^2) was performed 8 h-postinjection. Tumor volumes were measured once per day for 16 days. The values are presented as the mean with standard deviation for groups of three animals. On day 16, tumors and major organs were collected, weighed and processed for routine H&E staining. Finally, the images were taken by a Nikon light microscope (Nikon).

Immunohistochemistry

Tumor-bearing mice with i.v. injection of PBS, $HMoS_x$-HSA or O_2@PFH@$HMoS_x$-HSA were treated with or without NIR laser irradiation (670 nm, 1 W/cm^2, 5 min), respectively. After i.v. injection with pimonidazole hydrochloride (60 mg/kg) (Hypoxyprobe-1 plus kit, Hypoxyprobe Inc) for 30 min, the tumors were surgically excised. The pimonidazole hydrochloride could be reductively activated in hypoxic cells and formed stable adducts with thiol (sulphydryl) groups in proteins, peptides and amino acids. To explore the pimonidazole, frozen tumor sections were subsequently incubated with mouse anti-pimonidazole primary antibody (dilution 1:200, Hypoxyprobe Inc.) and FITC-conjugated goat anti-mouse secondary antibody (dilution 1:200, Beyotime). Moreover, cell nuclei were stained using DAPI. The images were obtained using a confocal microscope (Leica).

Results and Discussion

Preparation and Characterization of Nanoparticles

In this study, we developed a facile strategy for the preparation of hierarchical hollow MoS_x nanoparticles ($HMoS_x$) using NH_3 bubbles as soft template, which were produced under the solution-phase reaction. The procedure for the synthesis of $HMoS_x$-HSA is illustrated in Figure 1A. As shown in the transmission electron microscopy (TEM) image (Figure 1B), hollow nanospheres were observed with uniform size and shell thickness of ~140 nm and ~20 nm, respectively. In addition, the detailed morphology characteristics of all steps during the preparation are displayed in Figure S1, indicating the formation process of the hollow structure of the MoS_x. The high-resolution transmission electron microscopy (HRTEM) image of a partial enlargement of the shell (Figure S2A) indicated the amorphous state of $HMoS_x$, which was consistent with the X-ray diffraction (XRD) pattern (no obvious diffraction peak was observed) (Figure S2B). The prepared hollow MoS_x nanoparticles exhibited typical IV type of nitrogen adsorption-desorption isotherm (Figure 1C). In addition, the pore-size distribution (inset of Figure 1C) indicated that a maximum peak pore diameter was ~2.3 nm, further confirming their mesoporous nanoshell structure. From the isotherms curve, the specific surface area of those nanoparticles was calculated to be 72.5 cm^2g^{-1}, allowing the effective loading of guest molecules in the inner cavity of such hollow nanostructure.

In the second step, we firstly used lipoic acid (LA) containing a disulfide group and a carboxyl group on the two terminals, respectively, to functionalize the $HMoS_x$. The two sulfur atoms in the LA moiety enabled much stronger binding to $HMoS_x$ compared to the single thiol. Then the HSA protein was covalently conjugated to lipoic acid-coated $HMoS_x$ to enhance their stability and solubility via the formation of amide bonds between carboxylic groups in the lipoic acid and amino groups of HSA with the help of 1-ethyl-3-(3-dimethylaminopropyl) carbodimide (EDC). Fourier transform infrared spectroscopy (FTIR) and circular dichroism (CD) characterizations were adopted to examine the conformation of HSA and $HMoS_x$-HSA, respectively. As displayed in Figure S3A, the characteristic bands of $HMoS_x$-HSA were consistent with pure HSA, suggesting the presence of HSA on the surface of $HMoS_x$. As shown in Figure S3B, compared to the CD spectra of pure HSA, the peak at 221 nm in the CD spectra of $HMoS_x$-HSA remarkably vanished, demonstrating an increase in random coil structures [28].

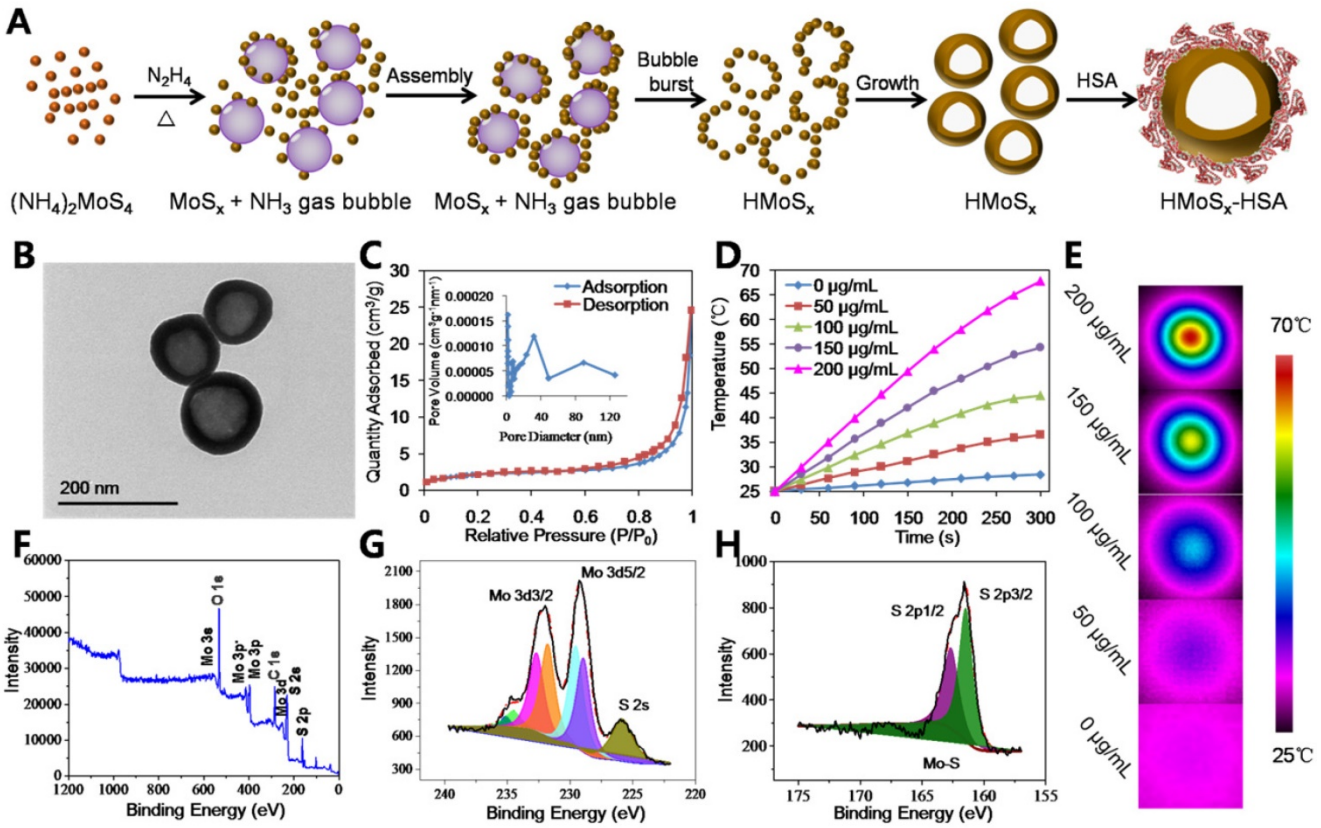

Figure 1. (A) A scheme showing the synthesis and surface modification of $HMoS_x$. (B) TEM images of the as-prepared $HMoS_x$ nanoparticles. (C) N_2 adsorption/desorption isotherm and corresponding pore-size distribution curves (inset) of $HMoS_x$ nanoparticles. (D) Temperature elevation curves of aqueous solutions containing $HMoS_x$-HSA with different concentrations under the irradiation of a 670 nm laser (1 W/cm²). (E) Photothermal images of $HMoS_x$-HSA dispersion at different concentrations over a period of 6 min following exposure to NIR laser (670 nm, 1 W/cm²). (F-H) XPS spectrum of the as-prepared $HMoS_x$ nanoparticles: (F) survey spectra, and high-resolution of (G) Mo 3d and (H) S 2p.

Interestingly, the as-prepared $HMoS_x$-HSA had a broad absorption in the NIR region from 600 nm to 1000 nm (Figure S4), which fitted well with the most common lasers used to investigate photothermal effects, e.g., 670 nm, 808 nm, and 980 nm. Under irradiation at 670 nm, the temperature of $HMoS_x$-HSA solutions reached 67.8 °C after 300 s, while the temperatures were 60.3 °C and 64.0 °C when exposed to 808 nm and 980 nm, respectively (Figure S5). This result showed that the 670 nm laser exhibited the highest photothermal efficiency for irradiating $HMoS_x$-HSA solution. Although the longer wavelengths (e.g., 808 nm, 980 nm) have a greater depth of penetration through body tissues than the shorter ones (e.g., 670 nm) [29], most photosensitizers, such as AlPc or Chlorin e6, can produce the PDT effect only under the irradiation of a 670 nm NIR laser. In addition, a single laser wavelength used for PTT and PDT simultaneously could avoid a relatively complicated treatment procedure and long therapeutic time [30]. In this case, a 670 nm laser was explored to provide both photothermal and photodynamic therapy for $HMoS_x$-HSA. To examine the photothermal effect of $HMoS_x$-HSA, we measured temperature trends in aqueous solutions of different concentrations of $HMoS_x$-HSA (0, 50, 100, 150, and 200 μg/mL) under the irradiation of a 670 nm NIR laser with a power density of 1 W/cm² (Figure 1D). The solution temperature rose rapidly and strongly depended on the concentration of $HMoS_x$-HSA, e.g., the temperature of $HMoS_x$-HSA solution (200 μg/mL) dramatically increased from 25.0 °C to 67.8 °C after laser irradiation for 300 s. Figure 1E presents photographs of different concentrations of $HMoS_x$-HSA captured by an infrared camera at 300 s. This result indicated their high photothermal conversion efficiency, which was calculated to be 39.6% (Figure S6).

To further determine the surface chemical composition and the valence state of Mo in the $HMoS_x$-HSA sample, X-ray photoelectron spectra (XPS) analysis was carried out. As shown in the XPS survey spectrum (Figure 1F), Mo, S, O, and C elements were detected respectively. As evident in Figure 1G, the high-resolution XPS spectrum of Mo contained Mo $3d_{3/2}$ peak and $3d_{5/2}$ peak at 231.80 eV and 228.78 eV as two rough peaks, respectively. These peaks were deconvoluted into several fine peaks of $Mo_{(IV)}$, $Mo_{(V)}$ and $Mo_{(VI)}$, which reflected the oxidation state of various Mo species in the

$HMoS_x$-HSA sample. The two peaks centered at 229.5 eV and 231.8 eV could be attributed to the bonding energies of $Mo3d_{5/2}$ and $Mo3d_{3/2}$ of $Mo_{(IV)}$, respectively, which matched with the spectra of MoS_2 [31]. The peaks at 235.15 eV and 228.9 eV were separately characteristic for $Mo3d_{3/2}$ and $Mo3d_{5/2}$ of $Mo_{(V)}$ [32]. In addition, binding energy values at 234.5 eV for $Mo3d_{3/2}$ level and 232.8 eV for $Mo3d_{5/2}$ level were observed, which corresponded to the standard values of $Mo_{(VI)}$ reported in literature [33]. Moreover, in the XPS spectrum of the S (Figure 1H), the two peaks at 162.70 eV and 161.30 eV corresponded to S $2p_{1/2}$ and S $2p_{3/2}$. By estimating the area ratio of $Mo_{(IV)}$, $Mo_{(V)}$ to $Mo_{(VI)}$ from XPS spectrum, we could conclude the x value in the $HMoS_x$-HSA sample was greater than 2 but less than 3 ($2<x<3$).

In this work, we aimed to prepare a potent nanoplatform that can act as a robust photosensitizer delivery carrier as well as an oxygen reservoir, allowing oxygen release in an oxygen deficient environment to enhance the photothermally activated PDT effect. Due to the large specific surface area and mesoporous shell structure of $HMoS_x$, the water-insoluble photosensitizer AlPc was loaded into the $HMoS_x$-HSA ($HMoS_x$-HSA/AlPc, Figure 2A). In this nanoparticle, both $HMoS_x$ and HSA could be used for drug loading. On one hand, the AlPc could be loaded on the surface of the $HMoS_x$ by π-π stacking [34]. On the other hand, the AlPc was able to be bound by the HSA via hydrophobic interaction between the drug molecule and the hydrophobic domain of the protein [35]. In addition, the AlPc could also enter into the mesoporous shell structure of the $HMoS_x$-HSA. The $HMoS_x$-HSA/AlPc nanoparticles were composed of C, N, Al, Mo, and S elements with an average size of ~145 nm (Figure S7 and S8). In addition, elemental mapping images (Figure 2B) and line scanning data of $HMoS_x$-HSA/AlPc nanoparticles further indicated the existence of Al, Mo, and S elements (Figure S9), suggesting the successful loading of AlPc. Besides, the UV-vis-NIR absorption spectrum of $HMoS_x$-HSA/AlPc showed an AlPc characteristic peak at ~670 nm, further indicating the existence of AlPc in the $HMoS_x$-HSA/AlPc nanospheres (Figure 2D). To investigate the possible drug loading ability of $HMoS_x$-HSA nanospheres, the $HMoS_x$-HSA solution (0.5 mg/mL) was impregnated with different amounts of AlPc (inset of Figure 2C). After removal of excess free AlPc molecules by centrifugal filtration, the UV-vis-NIR spectrum was recorded to examine the AlPc loading ratio (Figure 2C). It was found that the loading capacities of AlPc on $HMoS_x$-HSA increased as a function of drug amounts. The highest drug-loading ratio (weight ratios between the AlPc and $HMoS_x$-HSA) was determined to be ~74%. To investigate the photophysical and photochemical properties of $HMoS_x$-HSA/AlPc, the fluorescence intensity was observed using a fluorescence spectrophotometer (Figure 2E). Notably, when AlPc was loaded in $HMoS_x$-HSA, its intrinsic fluorescence signals were highly quenched owing to fluorescence resonance energy transfer (FRET) from AlPc to MoS_x. Moreover, perfuorohexane (PFH) can dissolve a large amount of oxygen due to the van der waals interaction between PFH and oxygen [36]. Due to the empty space in their hollow structure, the as-prepared $HMoS_x$-HSA nanoparticles can also be employed as carriers for loading PFH using the reported method [37]. A large number of bubbles emerged in the PFH-loaded $HMoS_x$-HSA/AlPc dispersion after heating over 60 °C (higher than the boiling point of perfuorohexane), indicating the potential oxygen-providing capability (Figure S10). In addition, the photothermal effect of O_2@PFH@$HMoS_x$-HSA/AlPc aqueous solutions with different concentrations of $HMoS_x$-HSA (0, 50, 100, 150, and 200 μg/mL) was also investigated under the irradiation of a 670 nm NIR laser with a power density of 1 W/cm^2 (Figure S11). The temperature of O_2@PFH@$HMoS_x$-HSA/AlPc solution (200 μg/mL) increased from 25.0 °C to 69.0 °C after the laser irradiation for 300 s, compared to 67.8 °C for $HMoS_x$-HSA solution with the same concentration (Figure 1D), which was ascribed to the presence of AlPc.

To be a potent nanomedicine, O_2@PFH@$HMoS_x$-HSA/AlPc should release O_2 and generate toxic reactive oxygen species at the tumor site rather than in the normal organs or bloodstream. Thus, we demonstrated a further therapeutic application of O_2@PFH@$HMoS_x$-HSA/AlPc that enabled activatable, on-site enhanced and oxygen self-enriched photodynamic therapeutics. First, AlPc-release behaviors were investigated with $HMoS_x$-HSA/AlPc incubated in 20% DMSO/PBS at 37 °C. As shown in Figure 2F, only 38.1% of AlPc was released within 24 h. However, the AlPc release from $HMoS_x$-HSA/AlPc under the 670 nm laser irradiation at 0 h and 1 h dramatically accelerated. More than 70.3% of loaded AlPc was released under irradiation by 670 nm laser at 24 h. Next, in order to examine the oxygen release, the nanoparticles with or without PFH loading were saturated with oxygen, and then added into deoxygenated water in a nitrogen-filled flask. Considering the fact that the oxygen could be consumed in the presence of AlPc under 670 nm laser irradiation, the O_2@$HMoS_x$-HSA or O_2@PFH@$HMoS_x$-HSA sample without AlPc was used in this experiment. The dissolved oxygen concentrations in those solutions were monitored by a portable oxygen meter in real time (Figure 2G). After addition of

O_2@$HMoS_x$-HSA and O_2@PFH@$HMoS_x$-HSA, sharply increased oxygen concentrations were observed for both solutions (initial peak in the blue and green line). Thereafter, since the two samples were placed in the oxygen-free solutions, the dissolved oxygen concentrations decreased overtime. Thus, PFH@$HMoS_x$-HSA was able to store more oxygen than $HMoS_x$-HSA alone, and could ensure gradual oxygen release to the surrounding hypoxic environment. In addition, after O_2@PFH@$HMoS_x$-HSA or O_2@$HMoS_x$-HSA was added into deoxygenated water, we used a 670 nm laser to irradiate the solution to investigate the influence of photothermal effect on oxygen release. Notably, when exposed to the laser, the O_2@PFH@$HMoS_x$-HSA solution displayed a sharp increase in oxygen concentration, indicating a burst release of oxygen from the nanoparticles. Considering the fact that $HMoS_x$-HSA showed no obvious shape or size changes after 670 nm irradiation (Figure S12), this burst release should be attributed to the increased temperature triggered by NIR-induced photothermal effect. For comparison, O_2@$HMoS_x$-HSA added solution presented less increase of oxygen concentration after the same laser irradiation. Since the released oxygen would be quickly diffused out under the nitrogen atmosphere, the oxygen concentrations might decrease at the later stage of continuous NIR irradiation. In fact, the real tumor is a relatively closed system, which is different from the solution sample tested here. Thus, the oxygen released from the nanosystem may probably stay in the tumor site for a much longer period of time to enhance the tumor oxygen status and the following PDT effect.

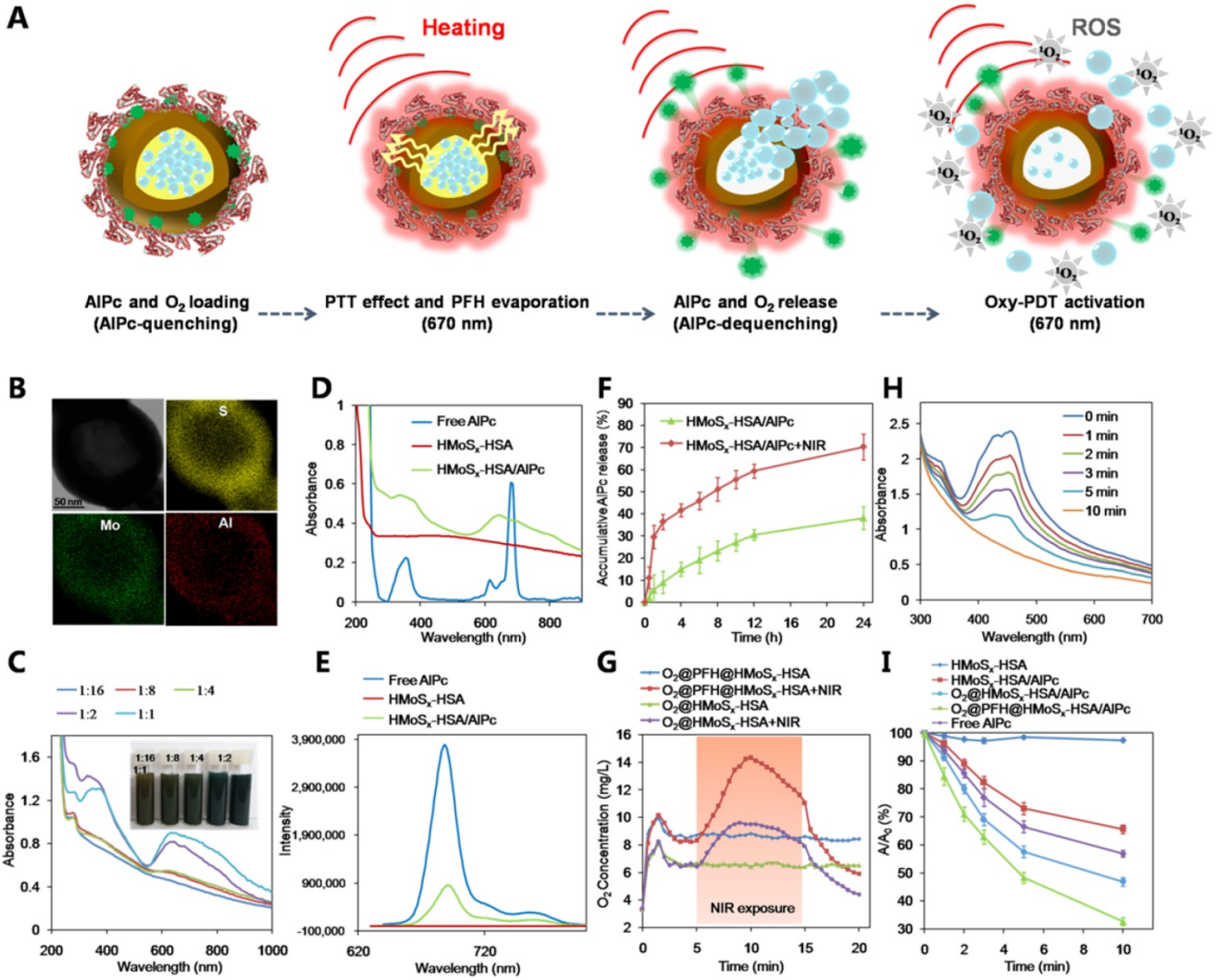

Figure 2. (A) Schematic illustration of the AlPc and O_2 release mechanism from O_2@PFH@$HMoS_x$-HSA/AlPc by sequential PTT/Oxy-PDT treatment. (B) HRTEM image of $HMoS_x$-HSA/AlPc nanoparticles. The element maps shown the distribution of S (yellow), Mo (green), and Al (red). (C) UV-vis-NIR spectra and photographs (inset) of $HMoS_x$-HSA/AlPc obtained at various AlPc loading concentrations after removal of excess free AlPc molecules. (D) UV-vis-NIR spectra and (E) Fluorescence spectra of free AlPc, $HMoS_x$-HSA and $HMoS_x$-HSA/AlPc in the aqueous solution. (F) In vitro release profiles of $HMoS_x$-HSA/AlPc in the absence or presence of 670 nm laser irradiation. (G) O_2 concentration change in different samples as indicated with or without NIR laser irradiation. (H) UV-vis-NIR spectra of mixture of O_2@PFH@$HMoS_x$-HSA/AlPc and DPBF exposure to 670 nm laser irradiation (1 W/cm²) for each time interval. (I) Singlet oxygen generation from different formulations in the presence of 670 nm laser.

Hypoxia (lack of oxygen) is usually considered as a characteristic of the tumor microenvironment, which contributes to the resistance to PDT since oxygen is an essential requirement in the process of PDT [38]. We then explored whether oxygen released from O_2@PFH@$HMoS_x$-HSA/AlPc would be favorable for laser-induced singlet oxygen generation by AlPc. Thus, the nanoparticles in an aqueous solution were irradiated with a 670 nm PDT laser. The singlet oxygen generation was monitored using 1,3-diphenyl isobenzofuran (DPBF) as a singlet oxygen indicator [39]. As shown in Figure 2H, the O_2@PFH@$HMoS_x$-HSA/AlPc sample exhibited a sharp decrease in DPBF absorbance at about 400 nm under 670 nm laser irradiation for 10 min. In addition, the singlet oxygen levels produced by different samples were also investigated (Figure 2I). Owing to the quenching effect of AlPc by $HMoS_x$ nanoparticles (Figure 2E), the singlet oxygen level produced by $HMoS_x$-HSA/AlPc (without O_2) was lower than free AlPc. Notably, after addition of O_2@PFH@$HMoS_x$-HSA/AlPc nanoparticles, sufficient O_2 could be quickly released, resulting in a remarkable enhancement of light-induced singlet oxygen generation by $HMoS_x$-HSA/AlPc. In contrast, no obvious change in singlet oxygen generation by $HMoS_x$-HSA was observed. Thus, it was expected that the Oxy-PDT effect of O_2@PFH@$HMoS_x$-HSA/AlPc would be significantly enhanced after exposure to the NIR laser.

Anticancer activity of the nanoparticles *in vitro*

In vitro experiments were then carried out to determine whether our nanoparticles would be an effective agent for synergistic PTT and Oxy-PDT. Considering the oxygen-dependent nature of PDT and the tumor microenvironment oxygen levels, 21% (normoxia) and 1% (hypoxia) oxygen levels were used in this experiment respectively. Firstly, the viabilities of the 4T1 cells treated with different samples with or without laser irradiation were determined by the methyl thiazolyl tetrazolium (MTT) assay. As shown in Figure 3A, the cell viability persisted more than 90% after treatment with O_2@PFH@$HMoS_x$-HSA/AlPc or NIR laser alone, suggesting their low cytotoxicity. After treatment with $HMoS_x$-HSA plus NIR laser irradiation (1 W/cm^2, 5 min), however, 40% of the cells were ruined due to the $HMoS_x$-induced PTT efficacy. Interestingly, $HMoS_x$-HSA/AlPc nanoparticles displayed a similar cytotoxicity to $HMoS_x$-HSA in the hypoxic condition after NIR laser exposure. While in the normoxic condition, the cytotoxicity of $HMoS_x$-HSA/AlPc nanoparticles with NIR laser was obviously increased, which indicated that the ROS generation depended on the oxygen concentration during the PDT treatment. When the O_2 was loaded into the $HMoS_x$-HSA/AlPc nanoparticles (O_2@PFH@$HMoS_x$-HSA/AlPc), the cytotoxicity was greatly enhanced regardless of the oxygen levels, suggesting that our optimal nanoparticles could successfully enrich oxygen to accelerate ROS generation even in the hypoxic environment. As presented in Figure 3C after laser irradiation, $HMoS_x$-HSA/AlPc nanoparticles showed a significant cytotoxicity in normoxic environment (21% O_2), while limited cytotoxicity in hypoxic incubator (<1% O_2) was detected even after exposure to the highest concentration, which was mainly attribute to the decreased ROS generation in the hypoxic medium. However, O_2@PFH@$HMoS_x$-HSA/AlPc nanoparticles displayed a similar cytotoxicity toward 4T1 cells in both hypoxic and normoxic medium after irradiation (Figure 3B), indicating successful acceleration of ROS generation in a hypoxic environment during oxygen enhanced PDT treatment.

Correspondingly, the PTT/Oxy-PDT efficacy was also evaluated in a visualized manner by live/dead staining, where live and dead cells were differentiated by co-staining with calcein AM (green fluorescence; living cells) and propidium iodide (PI) (red fluorescence; dead cells) in the hypoxic environment, respectively. As presented in Figure 3D, in the PBS or O_2@PFH@$HMoS_x$-HSA/AlPc alone treated groups, all of the cells exhibited green fluorescence, suggesting negligible damage effect from O_2@PFH@$HMoS_x$-HSA/AlPc alone. Under the NIR laser irradiation, a similar fluorescence distribution was observed in the $HMoS_x$-HSA/AlPc and $HMoS_x$-HSA treated group. Meanwhile, almost all of the cells incubated with O_2@PFH@$HMoS_x$-HSA/AlPc were killed and stained with red fluorescence after NIR laser irradiation. Taken together, these lines of evidence suggested the superior *in vitro* performance of O_2@PFH@$HMoS_x$-HSA/AlPc nanoparticles for combined PTT and Oxy-PDT treatment in vitro even in the hypoxic environment.

To further clarify the mechanism of cell death induced by our nanoparticles under laser irradiation, both early and late apoptotic cells were examined by flow cytometry [40] using Annexin-V-FITC/PI staining (Figure 3E). After treatment with O_2@PFH@$HMoS_x$-HSA/AlPc in the hypoxic condition, the population of apoptotic or dead cells was 83.2% after irradiation for 5 min (670 nm, 1 W/cm^2), which was much higher than $HMoS_x$-HSA/AlPc or $HMoS_x$-HSA treated groups. Moreover, in the control group of PBS or O_2@PFH@$HMoS_x$-HSA/AlPc without irradiation, negligible apoptotic or dead cells were found. The

above results indicated that O_2 played an important role in the PDT process combining O_2@PFH@HMoS$_x$-HSA/AlPc and laser irradiation.

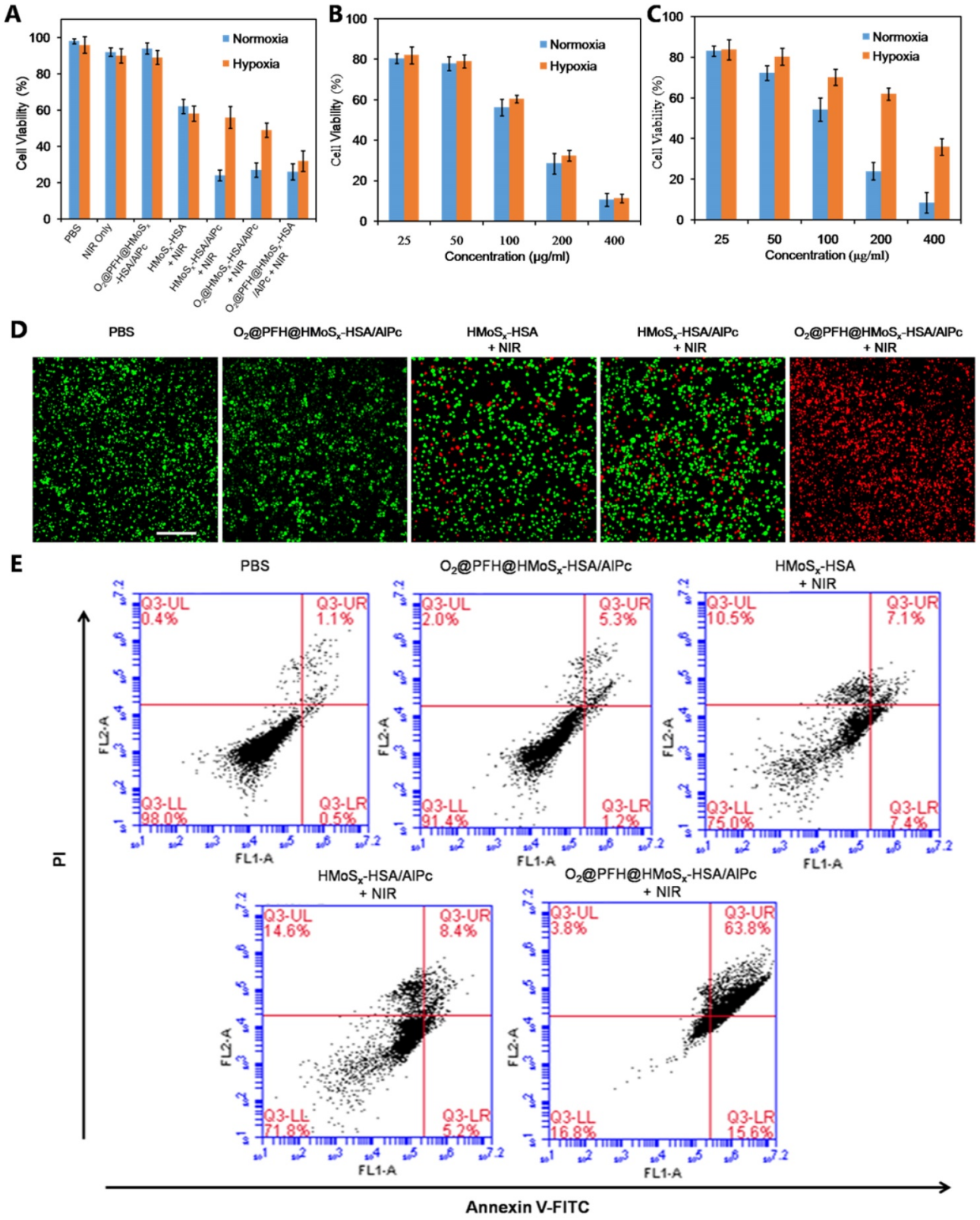

Figure 3. (A) Cell viability assay of 4T1 cells treated with different samples with or without NIR laser in hypoxic and normoxic environments. (B) Cell viability assay of O_2@PFH@HMoS$_x$-HSA/AlPc plus NIR treated 4T1 cells in hypoxic and normoxic environments. (C) Cell viability assay of HMoS$_x$-HSA/AlPc plus NIR treated cells in hypoxic and normoxic environments (D) Live-dead staining images of 4T1 cells treated with PBS, O_2@PFH@HMoS$_x$-HSA/AlPc, HMoS$_x$-HSA+NIR, HMoS$_x$-HSA/AlPc+NIR, or O_2@PFH@HMoS$_x$-HSA/AlPc+NIR, respectively, under a hypoxic condition. Scale bar: 500 μm. (E) Flow cytometry analysis of 4T1 cells after treatment with different samples under a hypoxic condition. Positive PI and Annexin V-Alexa Fluor 488 cells were defined as late apoptotic/necrotic cells.

Intracellular ROS generation by the nanoparticles

ROS-ID, a fluorogenic probe for intracellular hypoxia and ROS detection, was used to confirm the light-driven O_2 release and PDT enhancement of O_2@PFH@$HMoS_x$-HSA/AlPc nanoparticles. In this experiment, we analyzed ROS and hypoxia following laser irradiation by treating 4T1 cells with nanoparticles in the hypoxic and normoxic conditions respectively. As shown in Figure 4, in the normoxic environment, both O_2@PFH@$HMoS_x$-HSA/AlPc and $HMoS_x$-HSA/AlPc treated cells exhibited greatly enhanced ROS generation (green) upon NIR irradiation. Whereas in the hypoxic environment, low ROS production along with remarkable AlPc fluorescence (red) and pronounced hypoxia (magenta) were observed in $HMoS_x$-HSA/AlPc treated 4T1 cells after light irradiation. In contrast, O_2@PFH@$HMoS_x$-HSA/AlPc treated cells displayed a satisfactory ROS generation ability after light irradiation in hypoxic environment, indicating that O_2@PFH@$HMoS_x$-HSA/AlPc nanoparticles could overcome PDT-induced hypoxia.

In vivo FL/PA/CT triple-modality imaging

Multimodal imaging that combines the advantages of different imaging modalities can achieve more accurate detection of tumors [41]. Recently, considerable effort has been devoted to constructing functional nanoparticles with multimodal imaging capability [42]. Due to the loaded AlPc in our nanoparticles, the FL imaging capability of $HMoS_x$-HSA/AlPc nanoparticles was introduced using a 4T1 tumor-bearing nude mice model. After intravenous (i.v.) injection of free AlPc or $HMoS_x$-HSA/AlPc, fluorescence signal was recorded at 0, 4, 8, 12, and 24 h time points, respectively (Figure 5A). While a widely distributed fluorescence profile throughout the body was observed at the early stage post-injection. Sustained tumor accumulation of the $HMoS_x$-HSA/AlPc nanoparticles over time was discerned and reached a maximum at 8 h compared to other parts of the body (Figure 5A, top panel). At the same conditions, by contrast, the fluorescence images of mice with injection of free AlPc did not show tumor contrast obviously. To obtain clearer insight into the biodistribution of the $HMoS_x$-HSA/AlPc nanoparticles, major organs (heart, liver, spleen, lung, and kidney) and tumors were excised at 24 h post-injection. Notably, the $HMoS_x$-HSA/AlPc nanoparticles were primarily accumulated in the tumor while the free AlPc was mainly in the liver and kidney (Figure 5B, bottom panel). Semi-quantitative analyses based on ex vivo imaging of various tissues further confirmed the high tumor retention of $HMoS_x$-HSA/AlPc nanoparticle compared to other major organs (Figure S13A).

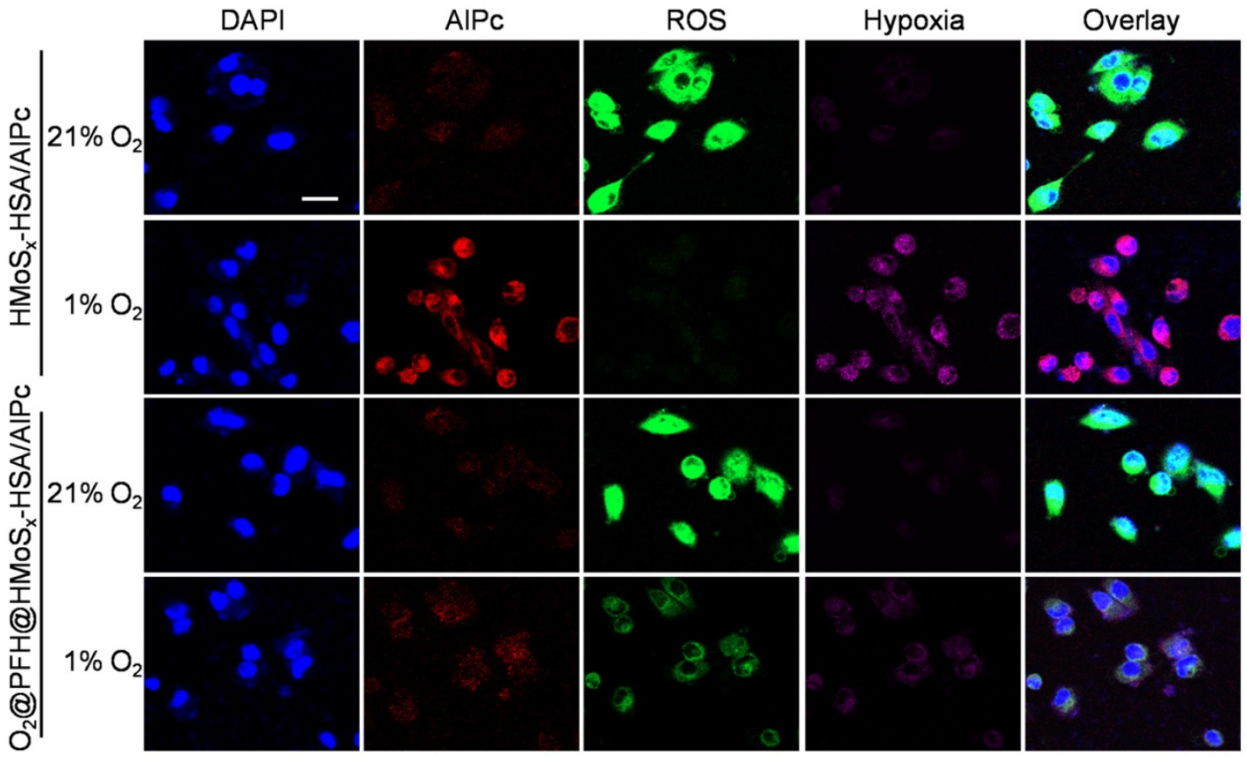

Figure 4. ROS and hypoxia generation following incubation of the cells with nanoparticles and laser irradiation. Confocal images of the cells stained with ROS and hypoxia probes. Cell nuclei were stained by DAPI, scale bar: 20 μm.

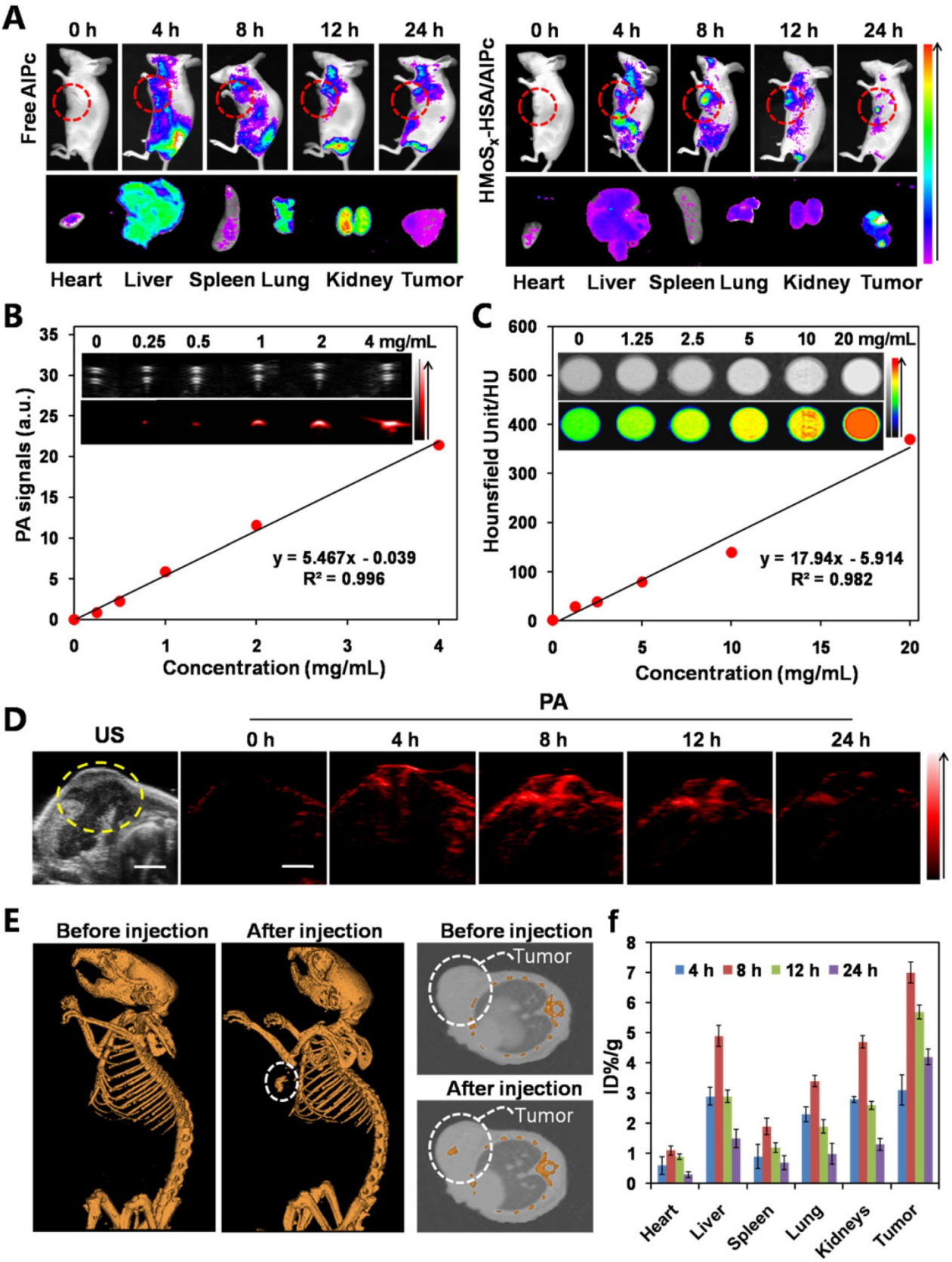

Figure 5. (A) Fluorescence images of Balb/c nude mice at different time points after administration of free AIPc and HMoS$_x$-HSA/AIPc; the bottom panel shows the ex vivo images examined at 24 h post-injection. (B) Photoacoustic intensity linearly fit to the concentration of HMoS$_x$-HSA/AIPc aqueous solutions; inset: the corresponding PA images. (C) CT signal intensity linearly fit to the concentration of HMoS$_x$-HSA/AIPc aqueous solutions; inset: the corresponding CT images. (D) Ultrasound (US) images and PA images of 4T1 tumor-bearing mice after being intravenously injected with HMoSx-HSA/AIPc at different time points. (E) In vivo CT images of tumors in mice before and after intratumor injection with HMoS$_x$-HSA/AIPc. (F) The biodistribution of HMoSx-HSA/AIPc measured at 4, 8, 12 and 24 h post i.v. injection.

Given the high tumor uptake of the $HMoS_x$-HSA/AlPc as revealed by FL imaging, we anticipated that the nanoparticles with strong NIR absorption would be excellent contrast agents for both in vivo and in vitro PA imaging. To verify this, we first investigated the potential of the $HMoS_x$-HSA/AlPc nanoparticles for in vitro PA imaging. As shown in Figure 5B, the $HMoS_x$-HSA/AlPc nanoparticles could induce intense optoacoustic signals, strictly following a concentration-dependent manner. For in vivo PA imaging, the mice were i.v. injected with the $HMoS_x$-HSA/AlPc nanoparticles (4 mg/mL, 200 μL) and imaged by a PA system at different time intervals. No obvious signal in the tumor region was observed before injection, while high PA contrast of the tumor was shown 8 h after injection (Figure 5D), suggesting the promising potential of $HMoS_x$-HSA/AlPc for real-time PA imaging for tumor diagnosis. In addition, the quantification of the PA signal intensity also showed that the maximal tumor uptake of $HMoS_x$-HSA/AlPc nanoparticles occurred at 8 h post-injection (Figure S13B), which was in good agreement with the FL imaging results. This time-dependent PA contrast indicated the gradual and efficient passively targeted accumulation of the $HMoS_x$-HSA/AlPc nanoparticles at the tumor site after systemic administration, making it possible to precisely track the agent's accumulation and evaluate the therapeutic efficacy.

Due to the large attenuation of X-rays by Mo [43], we also investigated the potential of the $HMoS_x$-HSA/AlPc for CT imaging. The CT contrast of the $HMoS_x$-HSA/AlPc nanoparticles was evaluated by acquiring phantom images of the nanoparticle dispersions with various concentrations in vitro (Figure 5C). It was found that the CT images became gradually brighter along with the increasing concentrations. Moreover, the calculated CT value (Figure 5C) revealed a linear increase with the concentration of nanoparticles. To confirm the performance of in vivo CT imaging, 4T1 tumor-bearing nude mice were intratumorally injected with the $HMoS_x$-HSA/AlPc nanoparticles (10 mg/mL, 50 μL), and then imaged using a small animal X-ray CT imaging system 1 h after injection. Compared with the images before injection, a strong tumor contrast was observed after injection (Figure 5E), confirming the excellent CT imaging capacity of the $HMoS_x$-HSA/AlPc nanoparticles. These results demonstrated the great potential of $HMoS_x$-HSA/AlPc nanoparticles as multifunctional contrast agents for in vivo imaging, which could be utilized to guide the laser irradiation in NIR light-driven therapy.

In order to quantitatively gain insight into the biodistribution of $HMoS_x$-HSA/AlPc nanoparticles in the mouse body, Mo content in tumors and major organs, including heart, liver, spleen, lung, and kidney, were determined via inductively coupled plasma mass spectrometry (ICP-MS). As shown in Figure 5F, high Mo content was found in tumor tissue at all tested time points, also indicating that $HMoS_x$-HSA/AlPc nanoparticles could be circulated to, and reside in the tumor. After 8 h injection, the Mo content in the tumor reached a maximum, which was in agreement with the FL and PA imaging data, suggesting the obvious tumor-homing effect of our nanoparticles.

In vivo antitumor efficacy

Encouraged by the photothermally triggered AlPc and O_2 release behavior of the O_2@PFH@$HMoS_x$-HSA/AlPc nanoparticles, we then investigated their feasibility for in vivo NIR laser-induced PTT/Oxy-PDT combination therapy. First, the photothermal effect of $HMoS_x$-HSA/AlPc nanoparticles was examined by using an infrared thermal camera. 4T1 tumor-bearing mice were intravenously injected with $HMoS_x$-HSA/AlPc nanoparticles (200 μL, 1 mg/mL) and exposed to a 670 nm laser at 8 h post-injection. It could be observed in Figure 6A that the temperature of the tumor rapidly increased to 60 °C within 5 min upon laser irradiation. To further assess the efficacy for laser-triggered synergistic therapy, O_2@PFH@$HMoS_x$-HSA/AlPc nanoparticles (200 μL, 1 mg/mL) were intravenously injected into 4T1 tumor-bearing mice. After being irradiated by the NIR laser (670 nm, 1 W/cm^2, 5 min) at 8 h post-injection, the tumor sizes were measured with calipers every two days (Figure 6C, bottom). On day 16, mice were sacrificed, and all tumors from different groups were collected and weighed (Figure 6C, top). Remarkably, tumors in the combination therapy group were completely eliminated on day 16 (Figure 6B and D). In contrast, solo photothermal therapy ($HMoS_x$-HSA+NIR group) had only moderate tumor growth inhibition. In addition, the survive ratio of the mice with the various treatments was also investigated. As shown in Figure S14, the control groups (PBS and O_2@PFH@$HMoS_x$-HSA/AlPc) exhibited early death as a function of time. Compared with control groups, $HMoS_x$-HSA+NIR and $HMoS_x$-HSA/AlPc+NIR treatment prolonged survival time to some extent (20% and 60%, respectively), which were still not satisfactory. As expected, O_2@PFH@$HMoS_x$-HSA/AlPc plus NIR laser performed the best antitumor efficiency with 100% survival rate up to 40 days. These observations indicated that the integration of photothermally activated Oxy-PDT into hyperthermia had the

potential to effectively inhibit the tumor growth and prolong the survival time through the synergistic therapeutic effect. Furthermore, hematoxylin and eosin (H&E)-stained images of collected tumor sections showed that the tumor cells in O_2@PFH@$HMoS_x$-HSA/AlPc+NIR group were severely destroyed, while no damage was detectable in PBS or O_2@PFH@$HMoS_x$-HSA/AlPc alone treated mice groups (Figure 6E). As shown in Figure S15, no noticeable damage was observed in main organs including heart, liver, spleen, lung and kidneys of O_2@PFH@$HMoS_x$-HSA/AlPc-injected mice after synergetic PTT/Oxy-PDT, suggesting that the optimal nanoparticles with excellent biocompatibility would be promising agents for NIR light-triggered synergistic PTT/Oxy-PDT tumor therapy.

To confirm the ability of oxygen release from O_2@PFH@$HMoS_x$-HSA nanoparticles to overcome hypoxia in vivo, a hypoxia-probe (pimonidazole) immuno-histochemical assay was performed by 4T1 tumors with different treatments. Immunofluorescence staining assay was carried out by staining the cell nuclei and hypoxic areas with DAPI (blue) and anti-pimonidazole antibody (green), respectively (Figure 7A, B). The 4T1 murine breast cancer tumors treated with $HMoS_x$-HSA+NIR showed weakened pimonidazole-stained (green) hypoxic signals compared with the control group, indicating that the tumor hypoxia could be partially reduced by the photothermal heating. More interestingly, the tumor treated with O_2@PFH@$HMoS_x$-HSA+NIR showed the lowest hypoxic signals among all different groups, demonstrating the remarkably enhanced tumor oxygenation owing to the combined effect of the photothermal heating as well as the NIR-triggered burst release of O_2 from PFH-loaded hollow nanoparticles.

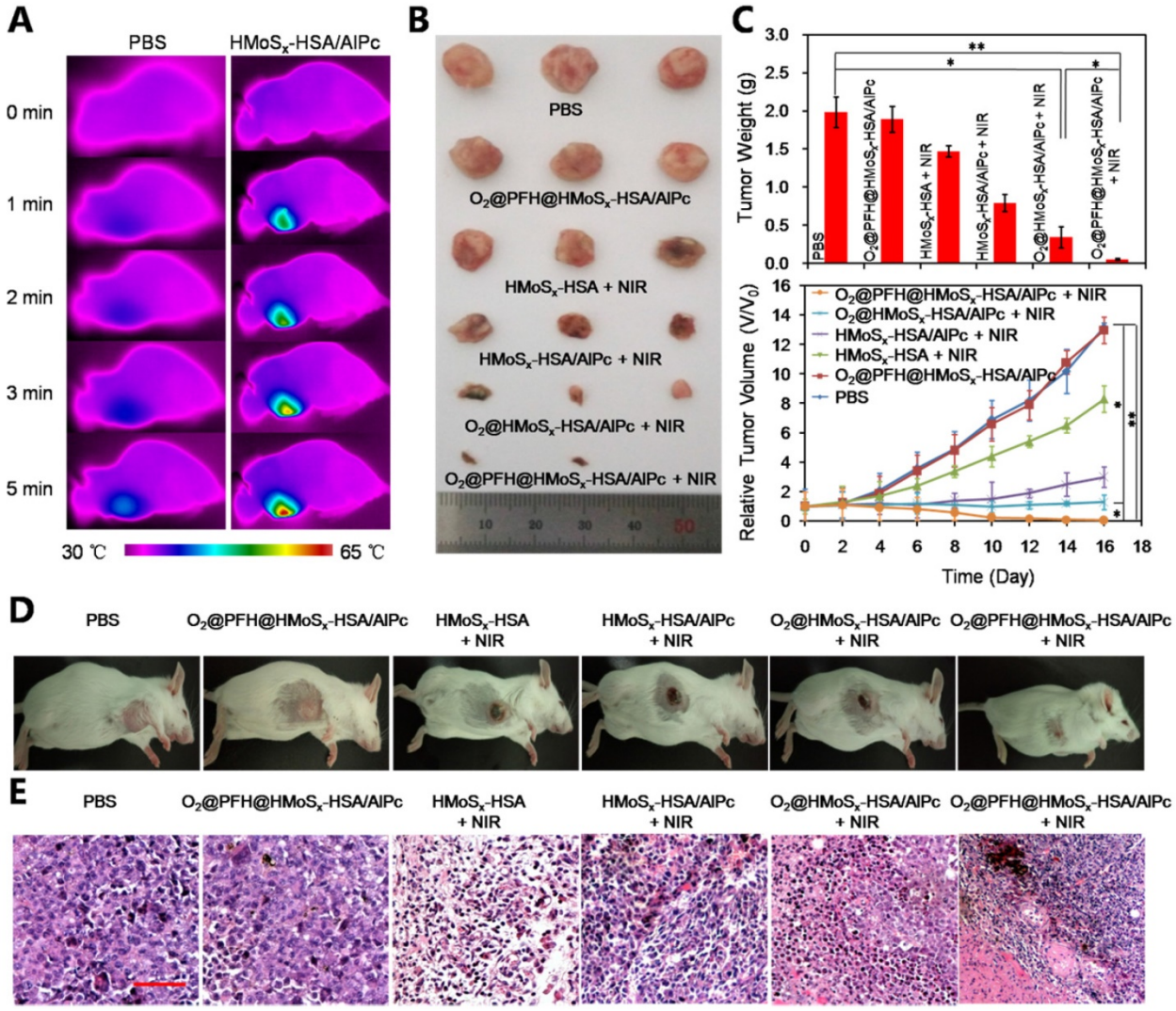

Figure 6. (A) Photothermal images of 4T1 tumor-bearing mice exposed to the NIR laser (670 nm, 1 W cm^{-2}, 5 min) after intravenous injection with PBS and $HMoS_x$-HSA/AlPc nanoparticles, respectively. (B) Photos of tumors collected from each group of the 4T1 tumor-bearing mice after various treatments. (C) Growth of 4T1 tumors in different groups of mice after treatment. The relative tumor volumes were normalized to their initial sizes. *P < 0.05, **P < 0.01. (D) Representative photos of mice 16 days after various treatments. (E) H&E-stained tumor slices collected from mice after treatment with different samples.

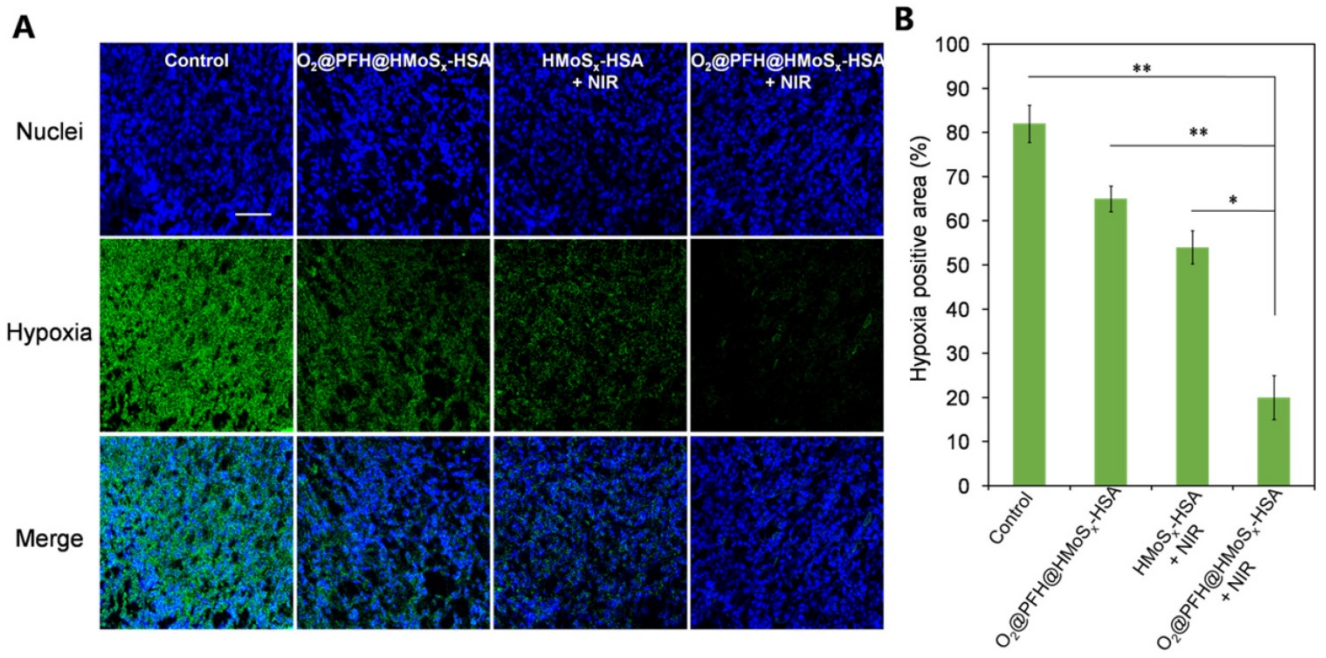

Figure 7. (A) Representative immunofluorescence images of tumor slices stained by the hypoxia-probe. The nuclei and hypoxic areas were stained with DAPI (blue), and anti-pimonidazole antibody (green), respectively. Scale bar: 200 μm. (B) Quantification of tumor hypoxia for different groups shown in (a). P values: *P < 0.05, **P < 0.01.

Conclusion

In this study, $HMoS_x$ nanoshells with hollow structure and mesoporous shells have been successfully fabricated via a rather simple, one-pot method, with HSA-modified on the surface. The strong NIR absorbance and high X-ray attenuation ability endow the $HMoS_x$-HSA nanoparticles with powerful capabilities for high-contrast PA and CT imaging. Meanwhile, the special hollow structure and mesoporous shell of $HMoS_x$-HSA can be utilized for efficient loading of O_2@PFH and AlPc. Under the single wavelength NIR laser irradiation (670 nm), $HMoS_x$ as a photothermal agent could concentrate absorbed light energy into heat and accelerate the AlPc and O_2 release from O_2@PFH@$HMoS_x$-HSA/AlPc, thus promptly activating the Oxy-PDT effect. The prepared $HMoS_x$-HSA nanoshell as an all-in-one nanoparticle formulation could thus serve as a multifunctional platform to integrate complementary imaging modalities and single wavelength laser maneuvered synergistic PTT/Oxy-PDT therapeutic strategies.

Abbreviations

$HMoS_x$: hollow MoS_x nanoparticles; PDT: photodynamic therapy; HSA: human serum albumin; PFH: perfluorohexane; AlPc: chloride aluminium phthalocyanine; FL: fluorescence; PA: photoacoustic; CT: X-ray computed tomography; Oxy-PDT: oxygen self-enriched photodynamic therapy; PTT: photothermal therapy; ROS: reactive oxygen species; PS: photosensitizers; NIR: near-infrared; EPR: enhanced permeability and retention; LA: lipoic acid; DPBF: 1,3-diphenyl isobenzofuran; PI: propidium iodide; TEM: transmission electron microscopy; HRTEM: high-resolution transmission electron microscopy; XRD: X-ray diffraction; EDC: 1-ethyl-3-(3-dimethylaminopropyl) carbodimide; FTIR: Fourier transform infrared spectroscopy; CD: circular dichroism; XPS: X-ray photoelectron spectra; FRET: fluorescence resonance energy transfer; MTT: methyl thiazolyl tetrazolium; ICP-MS: inductively coupled plasma mass spectrometry; H&E: hematoxylin and eosin staining.

Supplementary Material

Supplementary figures.
http://www.thno.org/v08p0955s1.pdf

Acknowledgements

This work was supported by the National Natural Science Foundation of China (81503016), Application Foundation and Cutting-edge Technologies Research Project of Tianjin (Young Program) (15JCQNJC13800), National Basic Research Project (973 Program) of China (2014CB932200), and Peiyang Young Talent Fund of Tianjin University (1701).

Competing Interests

The authors have declared that no competing interest exists.

References

1. Celli JP, Spring BQ, Rizvi I, Evans CL, Samkoe KS, Verma S, et al. Imaging and photodynamic therapy: mechanisms, monitoring, and optimization. Chem Rev. 2010; 110: 2795-838.
2. Agostinis P, Berg K, Cengel KA, Foster TH, Girotti AW, Gollnick SO, et al. Photodynamic therapy of cancer: an update. CA Cancer J Clin. 2001; 61: 250-81.
3. Foster TH, Gao L. Dosimetry in photodynamic therapy: oxygen and the critical importance of capillary density. Radiat Res. 1992; 130: 379-83.
4. Song X, Chen Q, Liu Z. Recent advances in the development of organic photothermal nano-agents. Nano Res. 2015; 8: 340-54.
5. Luo GF, Chen WH, Lei Q, Qiu WX, Liu YX, Cheng YJ, et al. A Triple-Collaborative Strategy for High-performance tumor therapy by multifunctional mesoporous silica-coated gold nanorods. Adv Funct Mater. 2016; 26: 4339-50.
6. Jordan B, Sonveaux P. Targeting tumor perfusion and oxygenation to improve the outcome of anticancer therapy1. Front Pharmacol. 2012; 3: 94.
7. Gordijo CR, Abbasi AZ, Amini MA, Lip HY, Maeda A, Cai P, et al. Hybrid nanoparticles: design of hybrid MnO2-polymer-lipid nanoparticles with tunable oxygen generation rates and tumor accumulation for cancer treatment. Adv Funct Mater. 2015; 25: 1857-72.
8. Huang CC, Chia WT, Chung MF, Lin KJ, Hsiao CW, Jin C, et al. An implantable depot that can generate oxygen in situ for overcoming hypoxia-induced resistance to anticancer drugs in chemotherapy. J Am Chem Soc. 2016; 138: 5222-5.
9. Fan W, Bu W, Shen B, He Q, Cui Z, Liu Y, et al. Intelligent MnO2 nanosheets anchored with upconversion nanoprobes for concurrent pH-/H2O2-responsive ucl imaging and oxygen-elevated synergetic therapy. Adv Mater. 2015; 27: 4155-61.
10. Prasad P, Gordijo CR, Abbasi AZ, Maeda A, Ip A, Rauth AM, et al. Multifunctional albumin-MnO2 nanoparticles modulate solid tumor microenvironment by attenuating hypoxia, acidosis, vascular endothelial growth factor and enhance radiation response. ACS Nano. 2014; 8: 3202-12.
11. Cheng L, Yuan C, Shen S, Yi X, Gong H, Yang K, et al. Bottom-up synthesis of metal-ion-doped WS2 nanoflakes for cancer theranostics nanoscale. ACS Nano. 2015; 9: 11090-101.
12. Teicher BA, Rose CM. Perfluorochemical emulsions can increase tumor radiosensitivity. Science. 1984; 223: 934-7.
13. Lee HY, Kim HW, Lee JH, Oh SH. Controlling oxygen release from hollow microparticles for prolonged cell survival under hypoxic environment. Biomaterials. 2015; 53: 583-91.
14. Song X, Feng L, Liang C, Yang K, Liu Z. Ultrasound triggered tumor oxygenation with oxygen-shuttle nanoperfluorocarbon to overcome hypoxia-associated resistance in cancer therapies. Nano Letters. 2016; 16: 6145-53.
15. Castro CI, Briceno JC. Perfluorocarbon-based oxygen carriers: review of products and trials. Artif Organs. 2010; 34: 622-34.
16. Cheng Y, Cheng H, Jiang C, Qiu X, Wang K, Huan W, et al. Perfluorocarbon nanoparticles enhance reactive oxygen levels and tumour growth inhibition in photodynamic therapy. Nat Commun. 2015; 6: 8785-92.
17. Fuchs J, Thiele J. The role of oxygen in cutaneous photodynamic therapy. Free Radic Biol Med. 1998; 24: 835-47.
18. Riess JG. Perfluorocarbon-based oxygen delivery. Artif Cells Blood Subst Biotechnol. 2006; 34: 567-80.
19. Riess JG. Understanding the Fundamentals of Perfluorocarbons and perfluorocarbon emulsions relevant to in vivo oxygen delivery. Artif Cells Blood Subst Biotechnol. 2005; 33: 47-63.
20. Song G, Liang C, Yi X, Zhao Q, Cheng L, Yang K, et al. Perfuorocarbon-loaded hollow bi2se3 nanoparticles for timely supply of oxygen under near-infrared light to enhance the radiotherapy of cancer. Adv Mater. 2016; 28: 2716-23.
21. Wang J, Tan X, Pang X, Liu L, Tan F, Li N. MoS2 quantum dot@polyaniline inorganic-organic nanohybrids for in vivo dual-modal imaging guided synergistic photothermal/radiation therapy. ACS Appl Mater Interfaces. 2016; 8: 24331-8.
22. Hirsch LR, Stafford RJ, Bankson JA, Sershen SR, Rivera B, Price RE, et al. Nanoshell-mediated near-infrared thermal therapy of tumors under magnetic resonance guidance. P Natl Acad Sci USA. 2003; 100: 13549-54.
23. Prodan E, Nordlander P, Halas NJ. Electronic structure and optical properties of gold nanoshells. Nano Lett. 2003; 3: 1411-5.
24. Elzoghby AO, Samy WM, Elgindy NA. Albumin-based nanoparticles as potential controlled release drug delivery systems. J Controlled Release. 2012; 157: 168-82.
25. Elsadek B, Kratz F. Impact of albumin on drug delivery-new applications on the horizon. J Controlled Release. 2012; 157: 4-28.
26. Zuo X, Chang K, Zhao J, Xie Z, Tang H, Li Bao, et al. Bubble-template-assisted synthesis of hollow fullerene-like MoS2 nanocages as a lithium ion battery anode material. J Mater Chem A. 2016; 4: 51-8.
27. Cai X, Jia X, Gao W, Zhang K, Ma M, Wang S, et al. A versatile nanotheranostic agent for efficient dual-mode imaging guided synergistic chemo-thermal tumor therapy. Adv Funct Mater. 2015; 25: 2520-9.
28. Sun SK, Dong LX, Cao Y, Sun HR, Yan XP. Fabrication of multifunctional gd2o3/au hybrid nanoprobe via a one-step approach for near-infrared fluorescence and magnetic resonance multimodal imaging in vivo. Anal Chem. 2013; 85: 8436-41.
29. Idris NM, Jayakumar MKG, Bansal A, Zhang Y, et al. Upconversion nanoparticles as versatile light nanotransducers for photoactivation applications. Chem Soc Rev. 2015; 44: 1449-78.
30. Jang B, Park JY, Tung CH, Kim IH, Choi Y. Gold nanorod-photosensitizer complex for near-infrared fluorescence imaging and photodynamic/photothermal therapy in vivo. ACS Nano. 2011; 5: 1086-94.
31. Yoon T, Kim KS. One-step synthesis of cos-doped β-Co(OH)2@amorphous mos2+x hybrid catalyst grown on nickel foam for high-performance electrochemical overall water splitting. Adv Funct Mater. 2016; 26: 7386-93.
32. Bao T, Yin W, Zheng X, Zhang X, Yu J, Dong X, et al. One-pot synthesis of pegylated plasmonic moo3-x hollow nanospheres for photoacoustic imaging guided chemo-photothermal combinational therapy of cancer. Biomaterials. 2016; 76: 11-24.
33. Bhosle V, Tiwari A, Narayan J. Epitaxial growth and properties of MoOx (2<x<2.75) films. J Appl Phys. 2005; 97: 083539.
34. Liu T, Wang C, Gu X, Gong H, Cheng L, Shi X, et al. Drug Delivery with PEGylated MoS2 Nano-sheets for Combined Photothermal and Chemotherapy of Cancer. Adv Mater. 2014; 26: 3433-40.
35. Chen Q, Wang C, Cheng L, He W, Cheng Z, Liu Z. Protein modified upconversion nanoparticles for imaging-guided combined photothermal and photodynamic therapy. Biomaterials. 2014; 35: 2915-23.
36. Lowe KC. Perfluorochemical respiratory gas carriers: benefits to cell culture systems. J Fluorine Chem. 2002; 118: 19-26.
37. Wang X, Chen H, Chen Y, Ma M, Zhang K, Li F, et al. Perfluorohexane-encapsulated mesoporous silica nanocapsules as enhancement agents for highly efficient High Intensity Focused Ultrasound (HIFU). Adv Mater. 2012; 24: 785-91.
38. Chen H, Tian J, He W, Guo Z. H2O2-activatable and O2-evolving nanoparticles for highly efficient and selective photodynamic therapy against hypoxic tumor cells. J Am Chem Soc. 2015; 137: 1539-47.
39. Wang J, Pang X, Tan X, Song Y, Liu L, You Q, et al. A triple-synergistic strategy for combinational photo/radiotherapy and multi-modality imaging based on hyaluronic acid-hybridized polyaniline-coated WS2 nanodots. Nanoscale. 2017; 9: 5551–64.
40. Thomas AP, Babu PSS, Nair SA, Ramakrishnan S, Ramaiah D, Chandrashekar TK, et al. Meso-tetrakis (p-sulfonatophenyl) N-confused porphyrin tetrasodium salt: a potential sensitizer for photodynamic therapy. J Med Chem. 2012; 55: 5110-20.
41. Lee DE, Koo H, Sun I, Ryu JH, Kim K, Kwon IC. Multifunctional nanoparticles for multimodal imaging and theragnosis. Chem Soc Rev. 2012; 41: 2656-72.
42. Kim J, Piao Y, Hyeon T. Multifunctional nanostructured materials for multimodal imaging, and simultaneous imaging and therapy. Chem Soc Rev. 2009; 38: 372-90.
43. Yin W, Yan L, Yu J, Tian G, Zhou L, Zheng X, et al. High-throughput synthesis of single-layer MoS2 nanosheets as a near-infrared photothermal-triggered drug delivery for effective cancer therapy. ACS Nano. 2014; 8: 6922-33.